Nanoscale

Room Temperature Doping of Ln3+ in Perovskite Nanoparticles: A Halide Exchange Mediated Cation Exchange Approach

Journal:	*Nanoscale*
Manuscript ID	NR-ART-01-2022-000490.R1
Article Type:	Paper
Date Submitted by the Author:	25-Mar-2022
Complete List of Authors:	Debnath, Gouranga; Chevron Science Center, Department of Chemistry Bloom, Brian; U Pittsburgh, Tan, Susheng; University of Pittsburgh, Petersen Institute of Nanoscience and Engineering; University of Pittsburgh, Electrical and Computer Engineering Waldeck, David; University of Pittsburgh, Department of Chemistry

Room Temperature Doping of Ln^{3+} in Perovskite Nanoparticles: A Halide Exchange Mediated Cation Exchange Approach

Gouranga H. Debnath,[1] Brian P. Bloom,[1] Susheng Tan[2,3] and David H. Waldeck[1,3,*]

[1]Department of Chemistry, University of Pittsburgh, Pittsburgh, Pennsylvania 15260, United States

[2]Department of Electrical and Computer Engineering, University of Pittsburgh, Pittsburgh, Pennsylvania 15261, United States

[3]Petersen Institute of NanoScience and Engineering, University of Pittsburgh, Pittsburgh, Pennsylvania 15261, United States

E-mail: dave@pitt.edu

* To whom correspondence should be addressed.

Keywords: Lanthanides, Perovskites, Nanoparticles, Ion Exchange, Doping

---

Abstract: This study presents a halide exchange mediated cation exchange strategy for a room temperature doping of trivalent lanthanide cations (Ln^{3+}) in cesium lead halide ($CsPbX_3$) nanoparticles (NPs). Post-synthetic addition of $LnCl_3$ [Ln = Nd, Sm, Eu, Tb, Dy, and Yb] to solution of $CsPbBr_3$ NPs generates the corresponding lanthanide doped NPs which display host sensitized Ln^{3+} emission. Structural and spectroscopic characterizations indicate a successful halide exchange and substitutional displacement of Pb^{2+} by Ln^{3+}. The effect of halide identity in controlling the Ln^{3+} sensitization was also evaluated. A photophysical framework is presented that can be used to predict the Ln^{3+} sensitization in perovskite NPs semiempirically, thereby removing the constraints of trial and error in designing a perovskite NP-Ln^{3+} host-guest combination.

Introduction: In the past six years, metal halide perovskite nanomaterials have emerged as a forefront of research in the fields of materials chemistry and spectroscopy alike,[1] primarily due to their large absorption cross sections, widely tunable emission properties (via quantum confinement effects and/or the modulation of halide composition),[2, 3] near-unity quantum yields (in cases),[4] high defect tolerance[5] and impressive charge carrier mobility.[6] Of particular interest is the generation of multicolor emission from perovskite nanomaterials for potential applications in sensors and optoelectronics, among others.[7-10] Doping transition metal ions like Mn^{2+}, which substitute for Pb^{2+} in the perovskite octahedra, has been heavily explored.[7-9] However, the broad emission profiles of transition metal ions and the sensitivity of their spectral properties to changes in the nanocrystal environment can greatly limit their applications.

Incorporating lanthanide cations (Ln^{3+}) in the perovskite matrix offers an interesting alternative by virtue of the unique spectroscopic properties of Ln^{3+}, in the form of sharp 4f-4f emission transitions that span the ultraviolet (UV), visible, and near-infrared (NIR) spectral region; long (microseconds to milliseconds) lifetimes, resistance to photobleaching, and the insensitivity of their spectral positions to changes in temperature or pH.[11, 12] While aliovalent doping was deemed not possible (by some workers)[13] during the early days of this subfield, many examples of aliovalent doping now exist. In 2017, Song and coworkers introduced a direct synthetic method for doping Ln^{3+} (Ln = Ce, Sm, Eu, Tb, Dy, Er and Yb) in to cesium lead chloride ($CsPbCl_3$) nanoparticles (NPs).[14] The $CsPbCl_3$ NPs were shown to act as a viable host and to sensitize the Ln^{3+} emission: an important requisite, considering the low oscillator strengths of Ln^{3+} ($< 10 M^{-1}cm^{-1}$ as compared to $10^4 - 10^5\ M^{-1}cm^{-1}$ for typical organic fluorophores) due to Laporte selection rules that greatly restrict their direct optical excitation.[11, 12]

Since that pioneering report, remarkable explorations into the photophysical properties of Ln^{3+} doped cesium lead halide NPs have been achieved. For example, the phenomenon of quantum cutting in Yb^{3+} doped perovskite NPs was first reported by Song and coworkers[15] and then followed by the report of Gamelin and coworkers[16, 17] showing a >100% emission quantum yield for Yb^{3+} in Yb-doped $CsPbX_3$ (X = Cl, Br). Also Fang and coworkers[18] demonstrated temperature dependent energy transfer for Eu^{3+} emission in $CsPbCl_{3-x}Br_x$:Eu NPs. Song and coworkers[19] studied the concentration dependent color tunability of Sm^{3+} in doped $CsPbCl_3$ NPs and demonstrated a white light LED. Noteworthy co-doped systems have also been reported, including $CsPbCl_{1.5}Br_{1.5}$: Yb^{3+}, Ce^{3+} NPs which utilize quantum cutting to improve the photoelectric conversion efficiency of commercial silicon solar cells from 18.1% to 21.5%,[15] Yb^{3+}-Er^{3+} codoped $CsPb(Cl_{1-x}Br_x)_3$ NPs that use host sensitization to boost the Er^{3+} emission at 1.5μm for applications in telecommunications,[20] and Mn^{2+} mediated energy transfer that switches on intense NIR emission for Nd^{3+}, Ho^{3+} and Er^{3+} in $CsPbCl_3$: Mn^{2+}, Ln^{3+} [Ln = Nd, Ho, and Er] NPs.[21]

An alternate protocol to the direct synthetic routes discussed for doping Ln^{3+} in perovskite NPs can be envisioned via a post-synthetic procedure. The post-synthetic introduction of Ln^{3+} in traditional II-VI semiconductor NPs and the investigation of their corresponding photophysical properties has been explored by us in detail.[22-24] However, reports on the post-synthetic Ln^{3+} doping at room temperature in perovskite NPs are scant, with studies mostly discussing Yb^{3+} doping in $CsPbX_3$ NPs (X = Cl, Br, I).[25, 26] This work describes a convenient post-synthetic strategy, which uses simultaneous halide and cation exchange, to generate Ln^{3+} [Ln = Nd, Sm, Eu, Tb, Dy, and Yb] doped $CsPbBr_3$ and $CsPbCl_3$ nanocrystals, which we refer to as $CsPbBr_3/LnCl_3$ and $CsPbCl_3/LnCl_3$. The Ln^{3+} used in this study possess one major luminescent energy level (*vide infra*). Novel benefits of this approach are:

(i) The ability to assess changes in properties (in our case the lanthanide luminescence sensitization) with doping conditions and to use the initial undoped system as a control for self-consistency.

(ii) A cocktail of Ln^{3+} (different lanthanides and different dopant densities) can be created from a single batch of undoped NPs. This allows a robust method to study the structural or photophysical properties in the doped versus undoped NPs, because it circumvents the pitfalls of synthetic heterogeneity that is often introduced when separate direct syntheses of Ln^{3+} doped NPs is undertaken.

(iii) The post-synthetic strategy allows one to simultaneously dope two Ln^{3+} of distinct identities in perovskite NPs thereby allowing multiplexing. We use this approach to examine the performance of perovskite NPs to sensitize the luminescence of different Ln^{3+} ions, and we present a photophysical framework that provides criteria for the selection of a perovskite(host)-Ln^{3+}(guest) combination to realize sensitized Ln^{3+} luminescence. This study provides a rational framework for expanding the scope of systems that can be created to study the photophysics of Ln^{3+} doped perovskite NPs.

Results and Discussion:

Halide Exchange. $CsPbBr_3$ NPs were synthesized based on literature reports;[2] see experimental section for details. Figure 1 shows transmission electron microscopy (TEM) images for the synthesized $CsPbBr_3$ NPs (Figure 1 a-c) and some of the Ln-doped NPs (Figure 1 d-g). The NPs display a cubic morphology with an average edge length of 6.5 ± 0.5 nm. The high-resolution TEM (HRTEM) images show lattice spacings (d-spacings) of 0.29 nm, 0.41 nm, and 0.58 nm that correlate to the (220), (020) and (110) planes of orthorhombic $CsPbBr_3$.[27, 28] Additional corroboration for this claim arises from the X-ray diffraction (XRD) patterns of the NPs (*vide*

infra). The TEM images following post-synthetic modification (see experimental section) of the $CsPbBr_3$ NPs by either $EuCl_3$ [Figure 1 (d,e)] or $YbCl_3$ [Figure 1 (f,g)], used as representative cases to highlight the generality for both visible and NIR emitting Ln^{3+}, preserves the overall dimension of the nanocubes with average edge lengths of 6.5 ± 0.6 nm for $CsPbBr_3/EuCl_3$ and 6.6 ± 0.4 nm for $CsPbBr_3/YbCl_3$ NPs.[3] The major difference however is observed in the HRTEM images, with the transformation of the d-spacings to 0.28 nm and 0.39 nm, which correlate to the (200) and (110) planes of cubic $CsPbCl_3$.[29] The XRD patterns of the $CsPbBr_3/LnCl_3$ NPs, discussed later, corroborate this structural transformation. These observations are in line with other halide exchange reactions reported for $CsPbX_3$ nanocubes.[3]

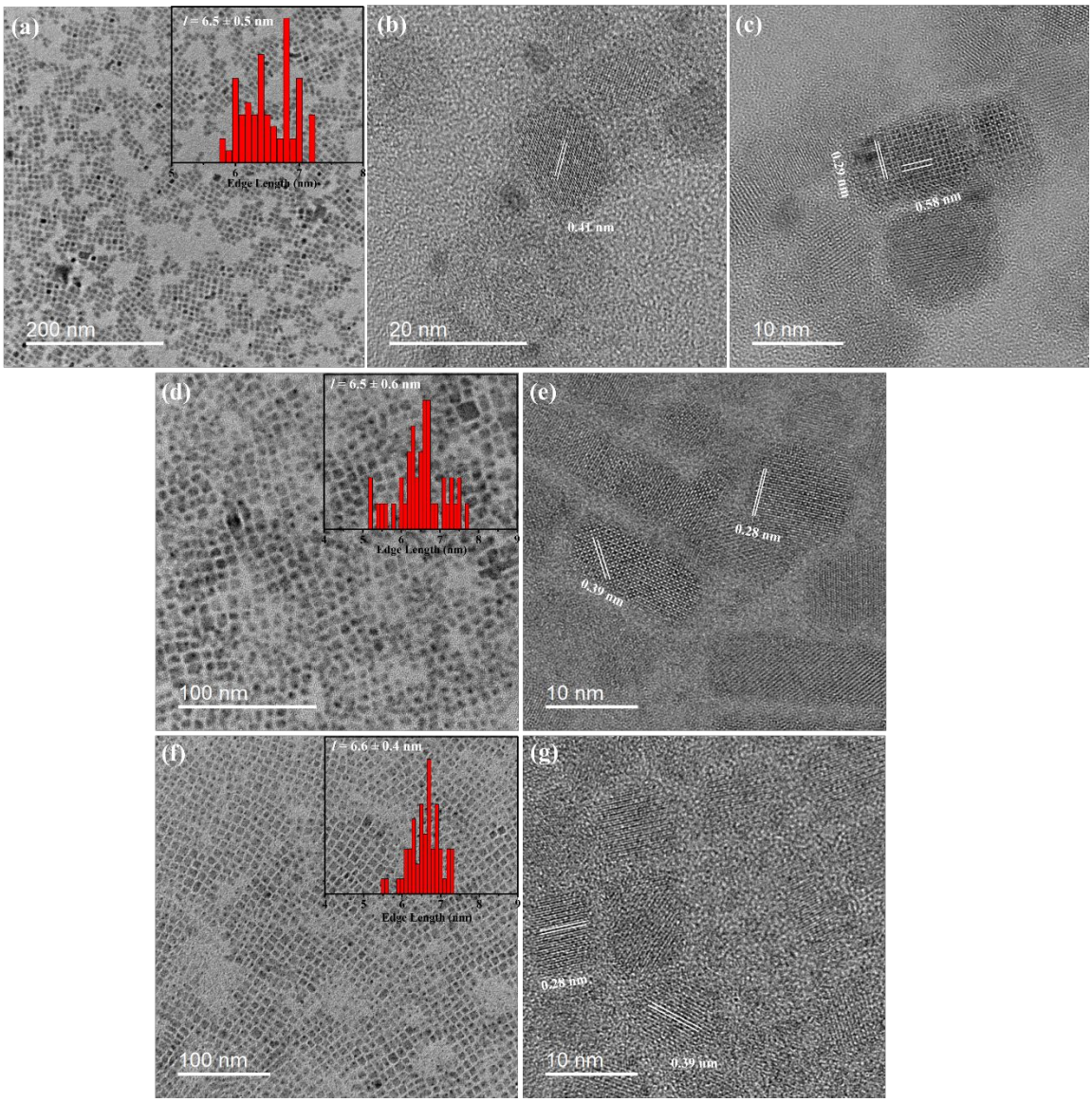

Figure 1. Panels (a-c) show TEM images along with the size distribution (inset) and the high resolution (HR) TEM images depicting the d-spacings of the $CsPbBr_3$ NPs, which are indicative of an orthorhombic crystal structure. Panels (d-e) show TEM, size distribution (inset), and HRTEM images of the $CsPbBr_3/EuCl_3$; and panels (f-g) show those for the $CsPbBr_3/YbCl_3$ NPs. The doped NPs in panels d through g conform to a cubic $CsPbCl_3$ crystal structure.

XRD patterns of the $CsPbBr_3$ NPs are shown in Figure 2 (left panel). The peaks at 2θ = 13.1°, 15.2°, 21.5°, 30.7°, 34.3°, 37.8° and 43.7° conform to the (101), (110), (020), (220), (130), (312) and (224) planes of orthorhombic $CsPbBr_3$, respectively (PDF: 01-072-7929).[27, 28, 30] Post-synthetic modification of $CsPbBr_3$ NPs by $LnCl_3$ [Ln = Nd, Sm, Eu, Tb, Dy, and Yb] changes the

XRD patterns consistently for all the different Ln ions (Figure 2, left and right panels) with new peaks appearing at 2θ = 15.8°, 22.4°, 27.5°, 31.9°, 35.8°, 39.3°, 45.7° and 48.7° which correspond to the (100), (110), (111), (200), (210), (211), (220) and (221) planes of cubic $CsPbCl_3$, respectively (PDF: 01-073-0692).[31] Together the TEM images and the XRD patterns indicate that the post-synthetic addition of $LnCl_3$ on the $CsPbBr_3$ NPs causes a structural change which is consistent with a halide exchange.

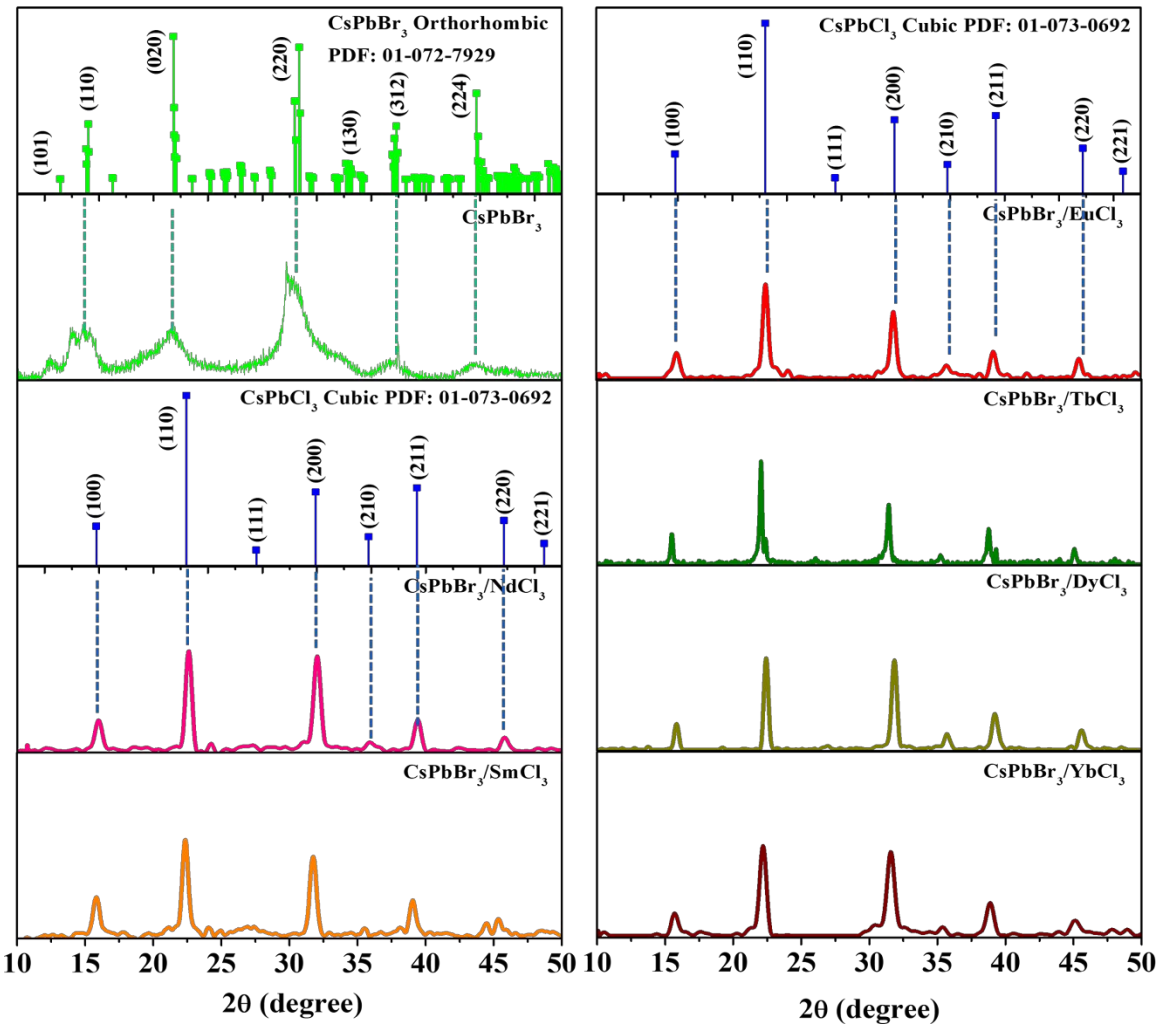

Figure 2. Experimental XRD patterns of $CsPbBr_3$ NPs and $CsPbBr_3/LnCl_3$ NPs [Ln = Nd, Sm, Eu, Tb, Dy, and Yb] are shown. For ease of comparison the powder diffraction files (PDF) for orthorhombic $CsPbBr_3$ and for cubic $CsPbCl_3$ are also plotted here. For clarity, the green and the blue dotted lines are shown for $CsPbBr_3$ NPs and $CsPbBr_3/LnCl_3$ NPs respectively to highlight the change in the diffraction patterns.

Halide Exchange, Cation Exchange and Ln^{3+} doping. Figure 3 (panels a-e) shows high-resolution XPS spectra of $CsPbBr_3/LnCl_3$ NPs (black, top) and $LnCl_3$ salts (blue, bottom); where Ln = Dy, Eu, Sm, Tb, and Nd respectively (see Figure S1 for the XPS spectra of $CsPbBr_3$ NPs). The XPS spectra confirm the presence and incorporation of Ln^{3+} in the perovskite matrix upon post-synthetic modification. Because of the extensive peak overlap between Yb4d, Br3p and Cl2p signals, meaningful interpretation was not possible for the Yb^{3+} case; and therefore spectra for $CsPbBr_3/YbCl_3$ and $YbCl_3$ salts are omitted. A red dashed vertical line is drawn on the spectra to illustrate that a modest core level shift occurs for Ln^{3+} between the $LnCl_3$ salt and the Ln doped perovskite. The core level shifts imply a change in electron density and further corroborate successful doping of the Ln into the perovskite framework. Peak position assignments associated with the different Ln oxidation states and any overlapping signatures in the spectral window are marked, when present, and coincide with previous reports.[32-34] For cases where strong spectral overlap with other signatures occurs, the samples were fit to a sum of peaks in which the orange peak corresponds to the Ln3d peak of interest, and the envelope is shown in green. The relative stoichiometric ratio of metal ions in the doped perovskites was determined using the integrated area of the photoelectron peaks, corrected for photoelectron yield (see Table 1).

To verify that the photoelectron yields were accurately calibrated, XPS measurements on $LnCl_3$ salts were performed and the stoichiometry was found to be as expected. Interestingly, for all $CsPbBr_3/LnCl_3$ NPs, the amount of Cs ≈ Pb + Ln while the Cs and Pb are in a nearly 1:1 ratio for the $CsPbBr_3$ nanocubes, i.e. the amount of Pb decreases in a manner proportional to the amount of incorporated Ln. The XPS measurements indicate a substitutional displacement of Pb^{2+} with Ln^{3+} while the XRD experiments clearly point to the halide exchange, when $LnCl_3$ is introduced to the $CsPbBr_3$ NPs post-synthetically.

Table 1. Stoichiometric ratio of the different elements before and after exchange are shown.[a]

System	Cs	Pb	Ln
$CsPbBr_3$	1.0	1.1	0.0
$CsPbBr_3/NdCl_3$	1.0	0.9	0.2
$CsPbBr_3/SmCl_3$	1.0	0.8	0.4
$CsPbBr_3/EuCl_3$	1.0	0.6	0.4
$CsPbBr_3/TbCl_3$	1.0	0.7	0.6
$CsPbBr_3/DyCl_3$	1.0	0.4	0.6

[a]The error in the calculation of the atomic percentage is ~10% which was propagated to ~14% while determining the stoichiometry.[35]

The Ln core level energies in the Ln doped perovskite are shifted from the positions found for the $LnCl_3$ salt, which indicates that the electronic environment of the Ln is different for the nanocube samples, and these shifts are consistent with doping in a perovskite. The analysis reveals a 2% to 8% incorporation of lanthanide ions into the NPs, see Table S1. Note the presence of Eu in the energy dispersive X-ray (EDX) spectrum of the $CsPbBr_3/EuCl_3$ NPs (Figure S15) which also corroborates the XPS results.

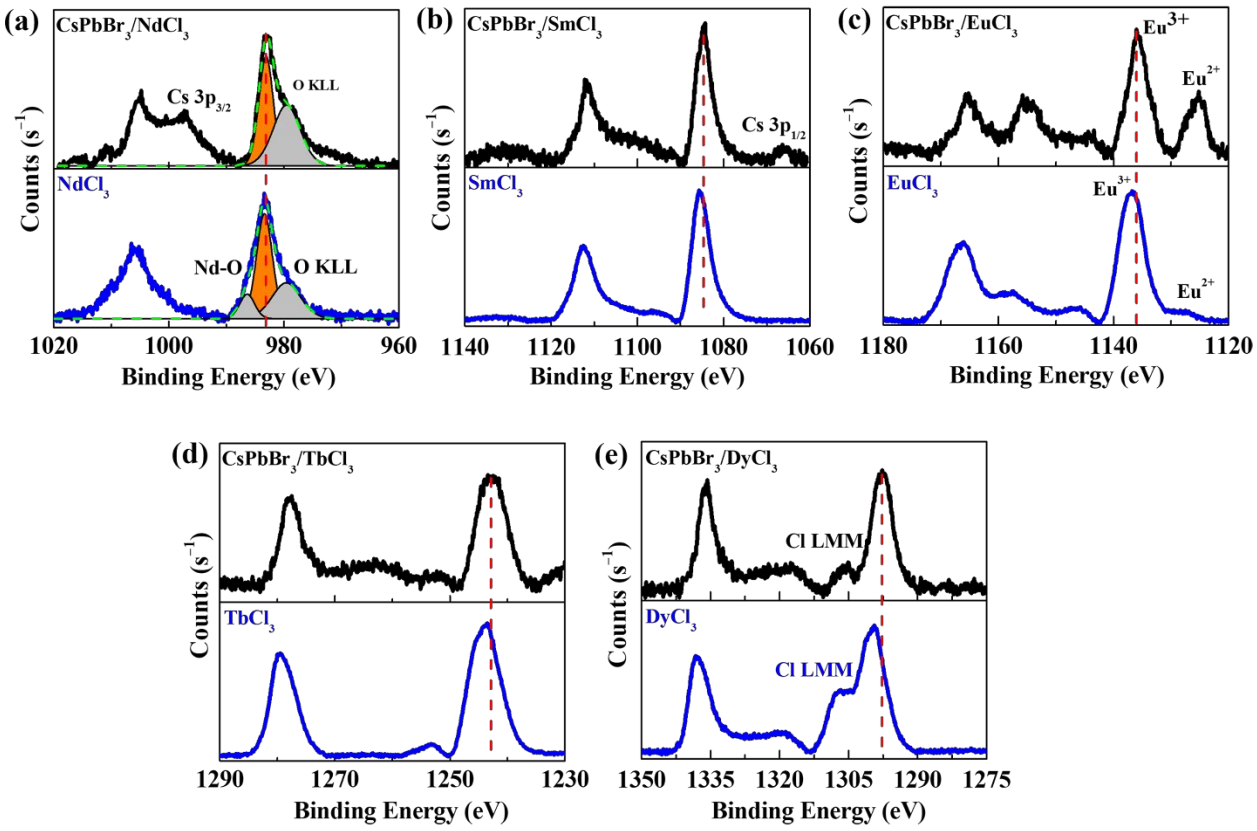

Figure 3. XPS spectra of $CsPbBr_3/LnCl_3$ NPs [Ln = Nd, Sm, Eu, Tb, and Dy] (black, top) and corresponding $LnCl_3$ salts (blue, bottom) used during the synthesis. Panels (a) through (e) correspond to Nd3d, Sm3d, Eu3d, Tb3d, and Dy3d respectively. Signatures arising from peaks other than lanthanides in the $3d_{5/2}$ region are marked. The red dashed line is used to illustrate the core level binding energy shift for the Ln ion upon incorporation into the perovskite lattice and the green dashed line in panel (a) is an envelope for the multicomponent fitting. Because of strongly overlapping regions, the data in panel (a) were fit to a sum of peaks and the peak of interest is highlighted in orange.

The TEM, XRD and XPS experiments establish the efficacy of the room temperature post-synthetic strategy used to dope Ln^{3+} in perovskite NPs without the formation of side products like $Cs(Ln)Cl_3$ or $Cs_4(Pb/Ln)Cl_6$.[36, 37]

Optical spectroscopy measurements were performed to investigate the photophysical properties of the $CsPbBr_3$ and $CsPbBr_3/LnCl_3$ NPs [Ln = Nd, Sm, Eu, Tb, Dy, and Yb] and to explore the Ln^{3+} emission properties (if any), following post-synthetic doping. The UV-vis absorption (490 nm) and steady-state emission (500 nm) spectra of the $CsPbBr_3$ NPs are shown in Figure 4a. The $CsPbBr_3$ NPs have emission quantum yields of 40% with an average lifetime of 2.35 ± 0.08 ns (see Figure S4 and Table S2) and are consistent with published reports.[2, 30] The halide exchange that follows the addition of $LnCl_3$ to the $CsPbBr_3$ NPs shifts the excitonic absorption and emission transitions to 405-410 nm and 410-415 nm respectively (Figure 4c-h).[3] This large shift is consistent with the substitution of Br by Cl in the NP lattice; $CsPbCl_3$ NPs display a 397 nm absorption peak and a 407 nm emission peak (*vide infra*). The minor shifts in the absorption and emission peaks for the different $CsPbBr_3/LnCl_3$ NPs likely result from the differences in the extent of the halide exchange (i.e., relative amounts of Br and Cl) and does not correlate with Ln^{3+} content or the effect of lanthanide contraction[14] (note the normalized absorption spectra of the $CsPbBr_3/LnCl_3$ NPs in Figure S16 which shows no trend as a function of Ln^{3+} atomic number). The excitonic emission transition in the $CsPbBr_3/LnCl_3$ NPs display quantum yields of 2-3% and average lifetimes of 0.5-0.6 ns (see Figure S4 and Table S2), which are also consistent

with that observed for $CsPbCl_3$ NPs (Figure 4b). These observations demonstrate that the perovskite's exciton emission properties are not affected strongly by the Ln doping but do change significantly with halide composition.

In addition to the NP exciton emission, all the Ln^{3+} doped NPs display lanthanide emission lines. The steady-state spectra of the $CsPbBr_3/TbCl_3$ NPs (Figure 4c) display Tb^{3+} emission bands at 490, 545, 585 and 620 nm that originate from the $^5D_4 \rightarrow {}^7F_J$ (J = 6–3) transitions.[11, 12, 24] The excitation spectra of the $CsPbBr_3/TbCl_3$ NPs, which are generated by monitoring the perovskite centered emission transition at 410 nm and the Tb^{3+} emission band at 545 nm, show significant overlap (see Figure S5), indicating that the host NP sensitizes the Tb^{3+} emission. The Tb^{3+} centered emission quantum yield was found to be 0.15–0.2%. A similar mechanism appears to operate for the $CsPbBr_3/EuCl_3$ NPs (Figure 4d), which display Eu^{3+} emission bands at 590, 616 and 700 nm that correspond to the $^5D_0 \rightarrow {}^7F_J$ (J = 1, 2, 4) transitions (Eu^{3+} emission quantum yields range from 0.1–0.15%).[11, 12, 24] The excitation spectra obtained by monitoring the Eu^{3+} emission band at 616 nm and the exciton emission band at 410 nm show a strong overlap (see Figure S5) which confirms that the Eu^{3+} emission is sensitized by the host NP. The steady-state luminescence spectra for the $CsPbBr_3/SmCl_3$ and $CsPbBr_3/DyCl_3$ NPs display only the perovskite emission band (see Figures 4e-f), without any noticeable Sm^{3+} or Dy^{3+} emission transitions; however, time-gated spectra reveal weak emission lines from Sm^{3+} or Dy^{3+} (*vide infra*). Figure 4g shows the steady-state emission for Nd^{3+} from $CsPbBr_3/NdCl_3$ NPs with bands centered at 890, 1058 and 1350 nm; these bands are attributed to the $^4F_{3/2} \rightarrow {}^4I_J$ (J = 9/2, 11/2 and 13/2) transitions.[11, 12, 24] Two-dimensional photoexcitation profiles of $CsPbBr_3/NdCl_3$ NPs, which are obtained by monitoring the Nd^{3+} centered emission bands, are shown in Figure S6 and indicate that the host NP sensitizes the emission. The Nd^{3+} emission bands have a quantum yield of ≤0.05%, which is reflected in the low

signal-to-noise ratio of the photoluminescence spectra. Figure 4h shows the successful realization of Yb^{3+} emission (with a relative quantum yield of 5%) in $CsPbBr_3/YbCl_3$ NPs. The emission band centered at 980 nm originates from the $^2F_{5/2} \rightarrow {}^2F_{7/2}$ transition.[11, 12, 24] The excitation map shown in Figure S7 clearly indicates an overlap with the $CsPbBr_3/YbCl_3$ NP absorption, thereby confirming host sensitization as the source for triggering the Yb^{3+} emission.

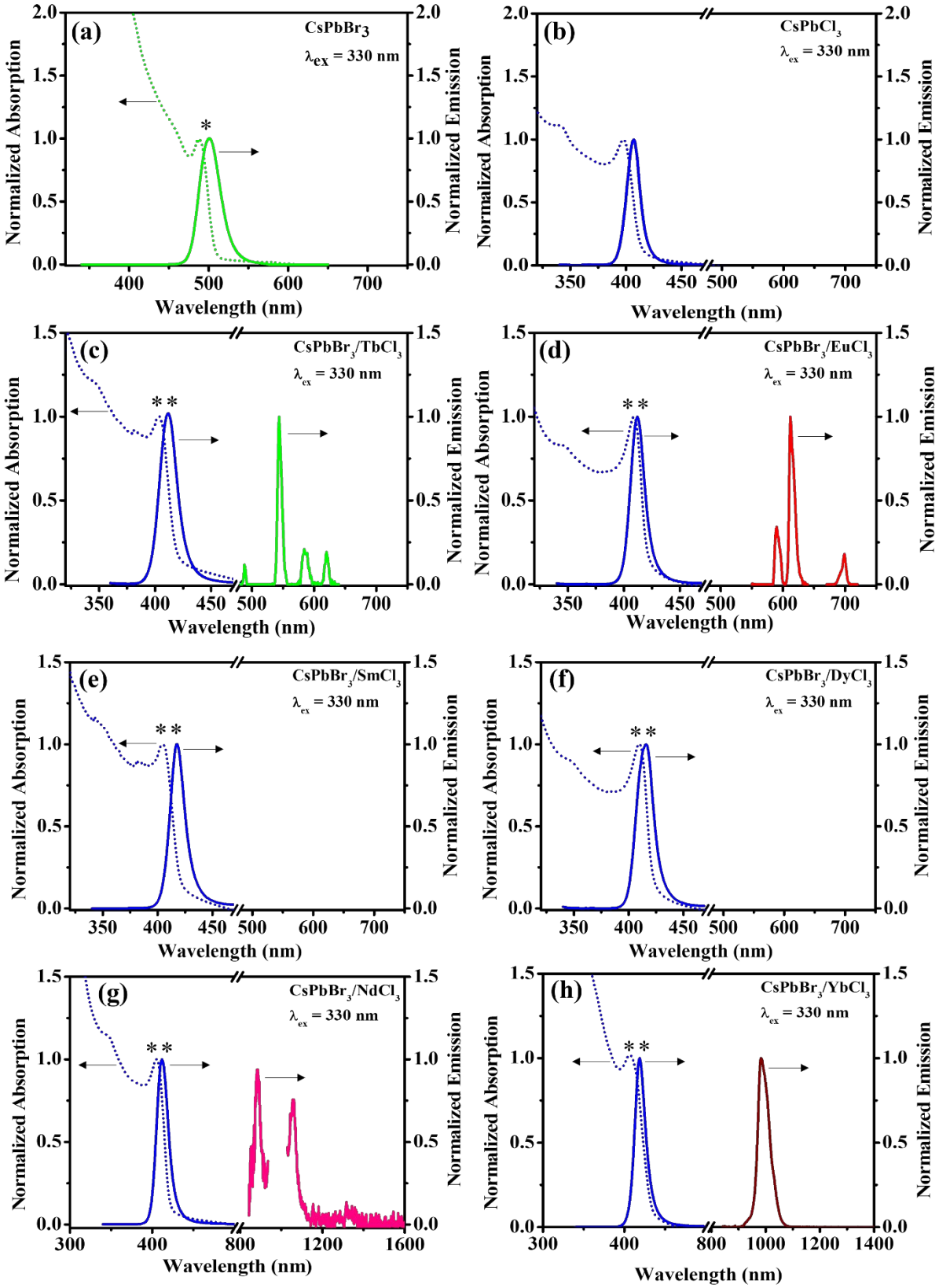
(a)
CsPbBr3
λex = 330 nm
(b)
CsPbCl3
λex = 330 nm
(c)
CsPbBr3/TbCl3
λex = 330 nm
(d)
CsPbBr3/EuCl3
λex = 330 nm
(e)
CsPbBr3/SmCl3
λex = 330 nm
(f)
CsPbBr3/DyCl3
λex = 330 nm
(g)
CsPbBr3/NdCl3
λex = 330 nm
(h)
CsPbBr3/YbCl3
λex = 330 nm
Normalized Absorption
Normalized Emission
Wavelength (nm)

Figure 4. UV-visible absorption and steady-state emission spectra of the $CsPbBr_3$ NPs (panel a), $CsPbCl_3$ NPs (panel b) and $CsPbBr_3/LnCl_3$ NPs [Ln = Tb, Eu, Sm, Dy, Nd, and Yb] (panels c-h) are shown. The NPs are dispersed in toluene. The emission spectra are collected using an excitation wavelength of 330 nm. The region between 940-1030 nm for the $CsPbBr_3/NdCl_3$ NPs and between 650-670 nm for the $CsPbBr_3/EuCl_3$ NPs is broken to eliminate harmonic from the excitation source. The sole contribution of the Tb^{3+} and Eu^{3+} has been extracted from their respective steady-state spectrum and presented in panels (c) and (d). A high energy excitation has been shown to be effective in realizing sensitized Ln^{3+} luminescence in semiconductor NPs.[24, 38] The (∗) and the (∗∗) have been added to signify the changes in the spectra from $CsPbBr_3$ NPs to $CsPbBr_3/LnCl_3$ NPs.

The steady-state photoluminescence experiments identify host sensitized Ln^{3+} emission from $CsPbBr_3/LnCl_3$ NPs [Ln = Nd, Eu, Tb, and Yb] while no emission was observed from the Sm^{3+} and Dy^{3+} counterparts. Because of the large difference in the radiative rates of the perovskite NPs (in nanoseconds) and the Ln^{3+} (in microseconds to milliseconds),[2, 24] the weak emission from lanthanide ions can sometimes be masked by a stronger NP exciton emission. Thus, time-gated spectra were collected for the Ln-doped NPs over a time window of 0.2 msec to 5 msec, which should eliminate the strong NP emission signal yet collect the long lived Ln^{3+} luminescence (see Figure 5).[24, 39-41] The Tb^{3+} emission from the $CsPbBr_3/TbCl_3$ NPs with bands at 490, 545, 585 and 620 nm that originate from the $^5D_4 \rightarrow {}^7F_J$ (J = 6–3) transitions is shown in Figure 5a, and the Eu^{3+} emission from the $CsPbBr_3/EuCl_3$ NPs with typical bands at 590, 616 and 700 nm that correspond to the $5D_0 \rightarrow {}^7F_J$ (J = 1, 2, 4) transitions is shown in Figure 5b. The excitation spectra, generated by monitoring the Eu^{3+} band at 616 nm display a profile with two bands centered at 390 nm and 330 nm that is bereft of the typical sharp direct excitation bands of their corresponding Ln^{3+} salts. The unmistakable overlap of these bands with NP absorption and steady-state excitation spectrum (see Figure S5) confirms the operation of host sensitization. Similarly, the excitation spectra generated on monitoring the Tb^{3+} emission band at 545 nm also confirms host sensitization. A detailed discussion on Tb^{3+} excitation profile is presented later. The time-gated spectra for the $CsPbBr_3/SmCl_3$ and $CsPbBr_3/DyCl_3$ NPs show discrete Sm^{3+} and Dy^{3+} emission bands. The

spectrum in Figure 5c, show Sm^{3+} emission bands at 564, 600, 650 and 710 nm and these bands can be assigned to the $^4G_{5/2} \rightarrow {}^6H_J$ (J = 5/2, 7/2, 9/2, and 11/2) transitions.[11, 12, 24, 42] The spectrum in Figure 5d shows Dy^{3+} centered emission bands at 475, 575, 660 and 750 nm that can be attributed to the $^4F_{9/2} \rightarrow {}^6H_J$ (J = 15/2, 13/2, 11/2, and 9/2) transitions of Dy^{3+}.[11, 12, 43] The excitation spectra monitoring the Sm^{3+} emission band at 650 nm and the Dy^{3+} emission band at 575 nm for the $CsPbBr_3/SmCl_3$ and $CsPbBr_3/DyCl_3$ NPs respectively, produce a broad profile that overlaps with the absorption band of the NPs, indicating that the luminescence is sensitized by the electronic states of the NP.

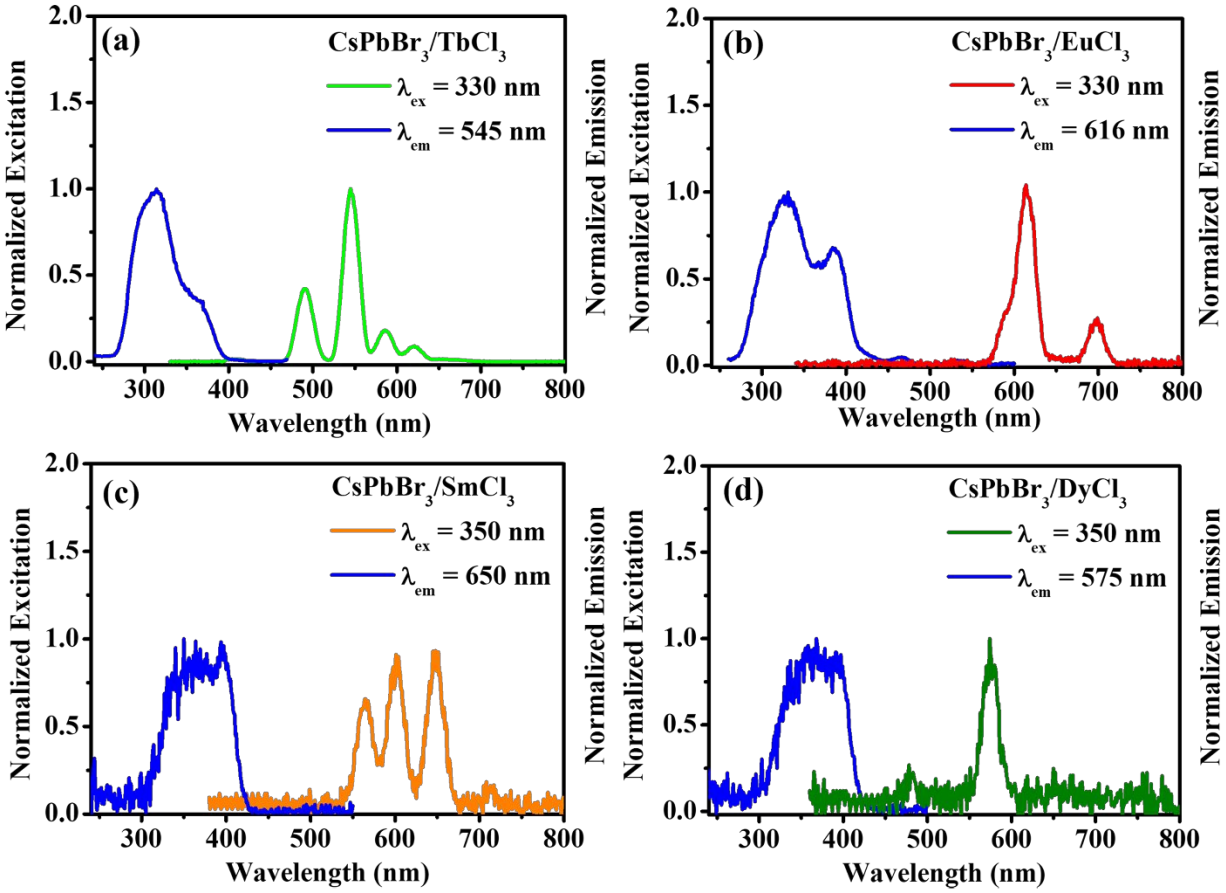

Figure 5. (a-d) Time-gated excitation and emission spectra of $CsPbBr_3/LnCl_3$ [Ln = Tb, Eu, Sm, and Dy] NPs are shown.

These observations unequivocally demonstrate the incorporation of Ln^{3+} in the perovskite host. The first report on size and charge mismatched Ln^{3+} doping into semiconductor NPs was shown by Petoud and coworkers for Tb^{3+} doped CdSe NPs.[40] Their excitation spectra, collected while monitoring the Tb^{3+} emission band at 545 nm, was shown to overlap with the excitation spectra of the CdSe itself, obtained while monitoring its bandgap emission at 500 nm, and its absorption spectrum. In contrast, excitation spectra for Ln^{3+} salts dissolved in solution are characterized by sharp excitation lines and is widely reported.[24] This pioneering work has been followed by many examples over the past decade on Ln^{3+} doped semiconductor NPs, such that the strong overlap of the excitation spectra, obtained while monitoring the Ln^{3+} emission bands, with the absorption (and excitation profiles) of the NP host is now taken to be strong evidence for successful Ln^{3+} incorporation.[22-24, 41, 42, 44-46]

The Role of Anion in Ln^{3+} Doping. The results discussed above show the dual halide and cation exchange when the $CsPbBr_3$ NPs are treated with $LnCl_3$. To better examine the role of the Cl anion in dictating the Ln^{3+} photophysics. $CsPbCl_3$ NPs were synthesized and treated post-synthetically with Ln^{3+} [Ln = Nd, Sm, Eu, Tb, Dy, and Yb] (see Experimental Section for details). The TEM image of the $CsPbCl_3$ nanocubes is shown in Figure 6a and have an average edge length of 7.6 ± 0.9 nm. A population of nanocube aggregates are also present and have not been considered in determining the size distribution. The HRTEM images (Figure 6b) show d-spacings of 0.28 nm and 0.39 nm which correlate to the (200) and (110) planes of cubic $CsPbCl_3$. The $CsPbCl_3/EuCl_3$ NPs (Figure 6c) show an increase in the average edge length of the cubes to 8.4 ± 0.9 nm. The UV-visible absorption spectra of the $CsPbCl_3$ and $CsPbCl_3$/Ln NPs further corroborate the doping induced increase in the NP edge length (*vide infra*). Like the $CsPbCl_3$ NPs, the $CsPbCl_3/EuCl_3$ NPs display a cubic crystal structure, as seen from the identical d-spacings

(Figure 6d). The XRD patterns of the $CsPbCl_3$ and $CsPbCl_3/LnCl_3$ NPs confirm the preservation of the crystal structure (Figure S8).

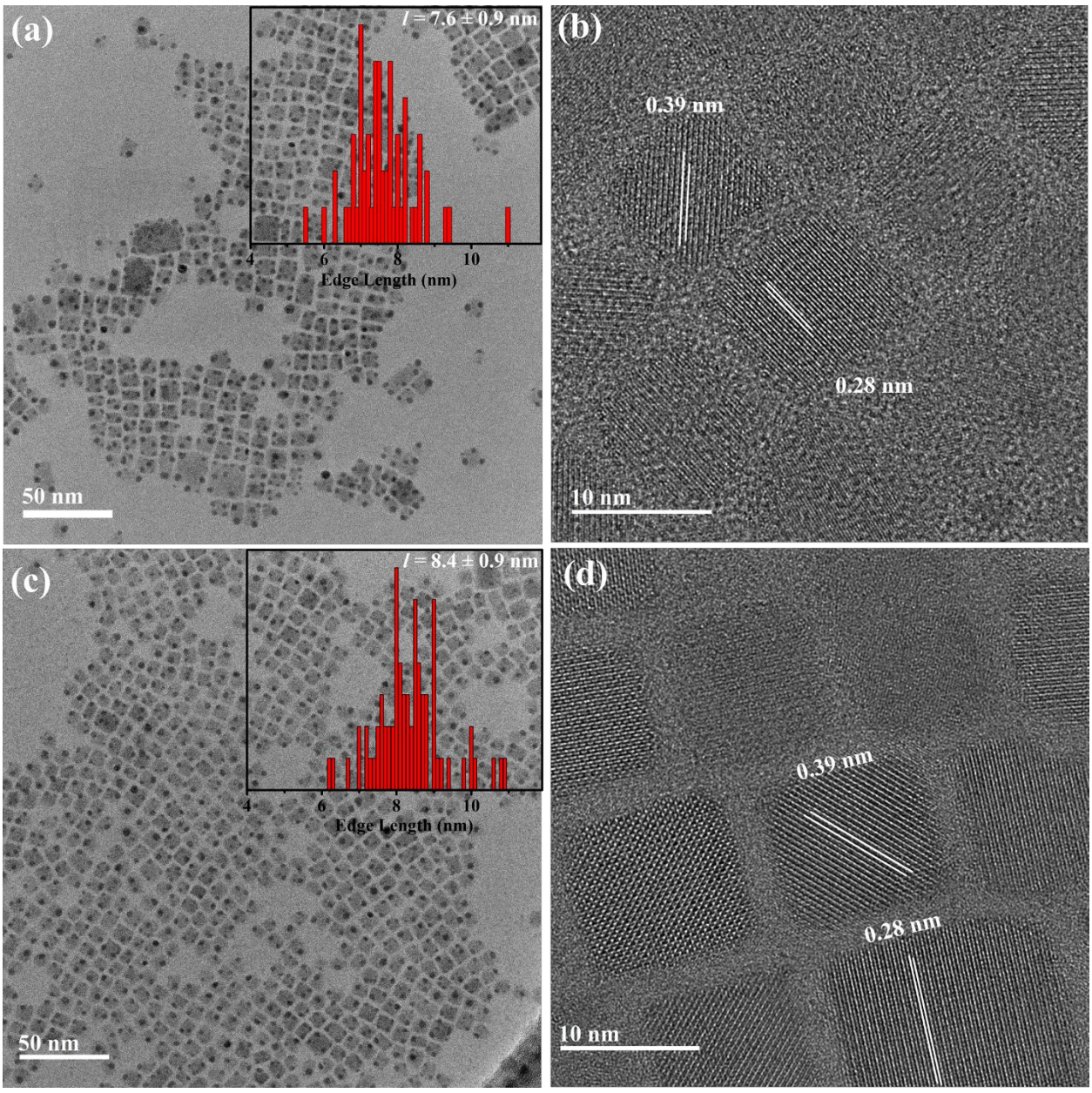

Figure 6. Panels (a-b) show a TEM image along with the size distribution (inset) and the high resolution (HR) TEM images depicting the d-spacings of the $CsPbCl_3$ NPs, indicative of a cubic crystal structure. Panels (c-d) show a TEM, size distribution (inset) and HRTEM images of the $CsPbCl_3/EuCl_3$ NPs. The doped NPs conform to the cubic crystal structure.

The photophysical properties of the $CsPbCl_3/LnCl_3$ NPs as a function of Ln^{3+} identity was studied using photoluminescence spectroscopy. Figure 7a shows the UV-visible absorption (397

nm) and emission spectra (407 nm) of the $CsPbCl_3$ NPs. The $CsPbCl_3$ NPs were found to have an emission quantum yield of 2% with an average lifetime of 0.37 ± 0.02 ns.[47] Addition of Ln^{3+} shifts the excitonic absorption and emission to 405 nm and 410 nm respectively (see Figures 7b and S9). The dopant induced red shift in the absorption and emission spectra of $CsPbCl_3$ NPs has been reported in previous studies.[48] The quantum yield of the $CsPbCl_3/LnCl_3$ NPs exciton emission are also seen to be about 2% with an average lifetime ranging from 0.4 – 0.7 ns (see Figure S10 and Table S3). Dopant induced passivation of the perovskite defects is argued to maintain the quantum yield along with an increased average lifetime in the $CsPbCl_3/LnCl_3$ NPs.[47] Exciting the $CsPbCl_3/YbCl_3$ NPs (Figure 7b) at 330 nm also generates the Yb^{3+} centered emission at 980 nm which originates from the $^2F_{5/2} \rightarrow {}^2F_{7/2}$ transition. The two-dimensional excitation map (Figure 7c) generated on monitoring the Yb^{3+} emission at 980 nm shows an overlap with the absorption spectrum of the $CsPbCl_3/YbCl_3$ NPs, confirming host sensitization. The steady-state absorption and emission spectra of the $CsPbCl_3/LnCl_3$ [Ln = Sm, Eu, Tb, and Dy] are shown in Figure S9. Time-gated excitation and emission spectra for the $CsPbCl_3/LnCl_3$ [Ln = Sm, Eu, and Tb] (Figure 7d-f) also confirm host sensitization leading to the observation of Tb^{3+} emission at 490, 545, 585 and 620 nm [originating from $^5D_4 \rightarrow {}^7F_J$ (J = 6–3) transitions]; Eu^{3+} emission at 590, 616 and 700 nm that correspond to the $5D_0 \rightarrow {}^7F_J$ (J = 1, 2, 4) transitions; and Sm^{3+} emission at 564, 600, 650 and 710 nm [assigned to the $^4G_{5/2} \rightarrow {}^6H_J$ (J = 5/2, 7/2, 9/2, and 11/2) transitions]. Interestingly, host sensitized emission for Nd^{3+} and Dy^{3+} was not observed for the $CsPbCl_3/Ln$ NPs [Ln = Nd and Dy]. This observation contrasts with their $CsPbBr_3/LnCl_3$ counterparts. Additional confirmation of Ln^{3+} incorporation in the $CsPbCl_3/LnCl_3$ NPs is shown by their XPS spectra (see Figures S11-S14 and Table S4).

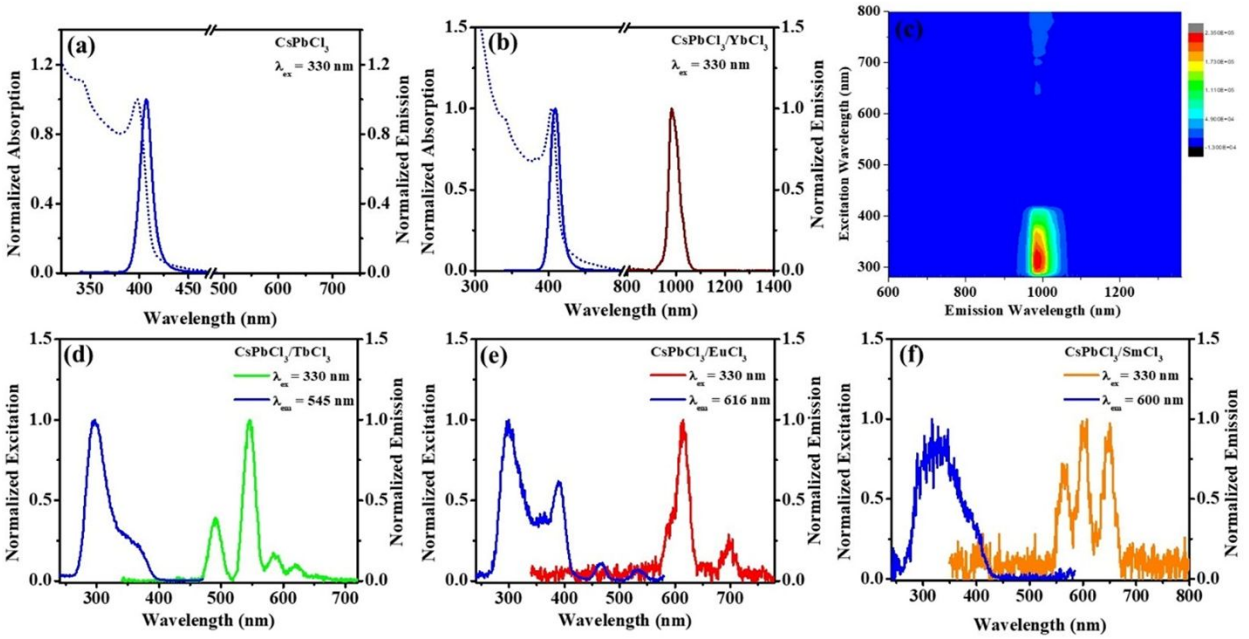

Figure 7. Panels (a-b) show the UV-visible absorption and steady-state emission spectra of the $CsPbCl_3$ and $CsPbCl_3/YbCl_3$ NPs. Panel (c) shows the 2D excitation map of the $CsPbCl_3/YbCl_3$ NPs generated by monitoring the Yb^{3+} emission at 980 nm. Panels (d-f) show the time-gated excitation and emission spectra of the $CsPbCl_3/LnCl_3$ NPs [Ln = Tb, Eu, and Sm].

A Photophysical Rationalization.

Phonon Emission Processes. A detailed investigation on the interplay of the different photophysical processes must be made to account for the differences in the degree of sensitization and/or realization of Ln^{3+} luminescence for the NP-Ln^{3+} combinations studied. The role of nonradiative deactivation of Ln^{3+} emission via phonon emission (similar to an internal conversion process in molecules) is an important process and has been used to explain the Ln^{3+} electronic transitions in $YAlO_3$ crystals.[49, 50] Additionally, multiphonon relaxation of Ln^{3+} excited states induced by solvent and ligand vibrations[51] and its implications for the Förster-Dexter energy transfer mechanism has also been explored extensively.[52, 53] Figure 8 shows an energy diagram of the Ln^{3+} electronic energy levels based on the Russell–Saunders coupling, in which some of the term symbols $^{2S+1}L_J$ of the levels are specified. The important parameter (ΔE_{phonon}) to consider is the energy gap between the Ln^{3+} emissive level (Ln^{3+}*, initial) and the highest spin orbit level of

the ground state multiplet (Ln^{3+}, final)[24, 42]; this energy gap parameter is listed in Table 2 for the different dopants. The nonradiative relaxation, indicated by the 'reaction'

$$\Delta E\ [Ln^{3+*} \rightarrow Ln^{3+}]\ \rightarrow Ln^{3+}\ (\text{dark}) + \Delta E_{\text{phonon,}}$$

must generate a large number of lattice phonons (or solvent) phonons. A larger ΔE_{phonon} requires larger nuclear distortions of the lattice and correlates to a lower propensity for undergoing nonradiative decay. For the visible emitting Ln^{3+}, a decreasing luminescence yield follows the order Tb > Eu > Dy ~ Sm and rationalizes the lower efficiency for sensitizing Sm^{3+} and Dy^{3+} emission. For the NIR emitting Ln^{3+}, the low luminescent yield of Nd^{3+} when compared to Yb^{3+} can be rationalized based on the large difference between their ΔE_{phonon} values.

Table 2. Energy parameter gauging the efficiency of environment induced quenching of Ln^{3+} emission.

Ln^{3+}	**Nd**	**Sm**	**Eu**	**Tb**	**Dy**	**Yb**
ΔE_{phonon} (cm^{-1}) [i, f]	5410	7400	12300	15100	7850	10240
i = initial state	$[^4F_{3/2}, {}^4I_{15/2}]$	$[^4G_{5/2}, {}^6F_{11/2}]$	$[^5D_0, {}^7F_6]$	$[^5D_4, {}^7F_0]$	$[^4F_{9/2}, {}^6F_{3/2}]$	$[^2F_{5/2}, {}^2F_{7/2}]$
f = final state						

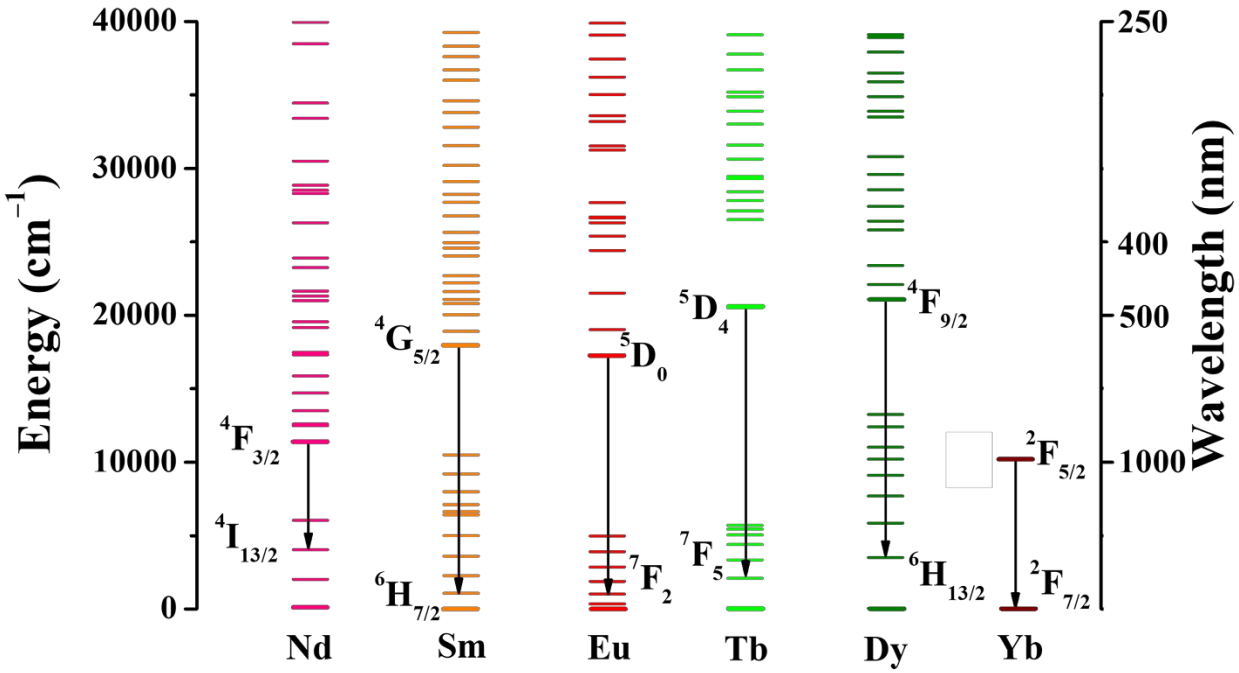

Figure 8. An energy diagram for Ln^{3+} (Ln = Nd, Sm, Eu, Tb, Dy, and Yb) is shown with the arrows indicating the generally most prominent emission transitions. The energy levels have been placed according to the reports by Rajnak and coworkers.[54-58]

Charge Trapping Model. An alternate approach to rationalize the differential sensitization efficiency of the Ln^{3+} in $CsPbBr_3/LnCl_3$ and $CsPbCl_3/LnCl_3$ NPs is through a charge trapping model where the Ln^{3+} ground and luminescent energy levels are placed at appropriate energies with respect to the valence and conduction band of the NP host (see Figure 9). The Ln^{3+} energy levels in this model act as sites which colocalize photogenerated electrons and holes. The colocalization of an electron and hole near these sites promotes their recombination by the population of the Ln^{3+} luminescent energy level, leading to the realization of sensitized Ln^{3+} luminescence. This mechanism has been used extensively over the past decade to predict the sensitization efficiencies of Ln^{3+} in doped II-VI sulfide and selenide NPs and in IV-VI oxide NPs.[23, 24, 41, 42, 45, 46, 59] The assignment of Ln^{3+} states acting as charge traps is not new and has been shown to explain the sensitization in Ln^{3+} doped bulk semiconductors. For example, Anderson and coworkers identified Tb^{3+} as a recombination center in ZnS and identified a donor level related

to Tb^{3+} [$6s^2 5d^1$] that lies 0.4 eV below the conduction band, while the $4f^8$ levels were assigned to be located somewhere below the valence band).[60] The report by Wen-lian and coworkers corroborate this mechanism.[61] Kimerling and coworkers[62] discuss the excitation of Er^{3+} in silicon and the energy transfer from shallow centers to Er^{3+} in a trap ionization process. A similar observation was also made by Langerak and coworkers on studying the excitation mechanism of Er in Si.[63] Scholz and coworkers assign Yb^{3+} as trap sites to explain the decay mechanism of Yb^{3+} luminescence in indium phosphide (InP).[64] Klik and coworkers[65] explained the Yb^{3+} sensitization in InP as excitation of the semiconductor and promotion of an electron from the valence band to the conduction band, followed by capture of an electron at the Yb^{3+} related trap and generation of an electron-hole pair on the trap site. A non-radiative recombination of the electron-hole pair excites the Yb^{3+} thereby generating the Yb^{3+} emission. A recent report by Weiss and coworkers also discusses Ln related defect states in $CsPbCl_3$ NPs.[66]

The method of constructing the energy level alignments in Figure 9 was adapted from the work of Dorenbos and coworkers[67, 68] which is based on the following assumptions:

(i) The core-like nature of the Ln^{3+} ion leads to a universal trend in their binding energies that is independent of the host.

(ii) The charge transfer energy (E_{CT}) from the anion valence band to the Eu^{3+} is equal to the energy difference between the valence band and the Eu^{2+} ground state.

Using these assumptions and the fact that the energy difference between the Eu^{3+} and the Eu^{2+} ground energy level is known to be about 5.7 eV for lower band gap materials,[68] it is only necessary to find E_{CT} for an energy level scheme.[67] The E_{CT} could not be determined experimentally here, so it was estimated from Pauling's electronegativity (η) scale and Jørgensen's relationship[69] according to the equation

$$E_{CT} = 3.72\ (\eta - 2)\ eV \quad (1)$$

Because the valence band in $CsPbCl_3$ has contributions from the Cl 3p and Pb 6s orbitals,[70] an average electronegativity of the Cl and Pb was used to estimate the E_{CT} (2.77 eV). The determination of E_{CT} at 2.77 eV was used to place the Eu^{2+} ground state which then sets placement of ground states for the other Ln^{2+} and Ln^{3+}.[67] Important parameters to consider are (a) ΔE_1 = [E(VB) – E(Ln^{3+})], which represents the energy offset between the valence band edge and the Ln^{3+} ground state (GS), and (b) ΔE_2 = [E(CB) – E(Ln^{3+}*)], which represents the energy offset between the conduction band edge and the Ln^{3+} luminescent state (LS). The compilation of ΔE_1 and ΔE_2 values for the Ln^{3+} are presented in Table 3.

Table 3. Energy Parameters for the $CsPbBr_3/LnCl_3$ and $CsPbCl_3/LnCl_3$ NPs.

Ln^{3+}	GS	LS	ΔE_1 (cm^{-1})[a]	ΔE_2 (cm^{-1})[b]
Nd	$^4I_{9/2}$	$^4F_{3/2}$	10,485	24,196
Sm	$^6H_{5/2}$	$^6G_{5/2}$	14,114	21,374
Eu	$^7F_0$	$^5D_0$	23,632	31,375
Tb	$^7F_6$	$^5D_4$	–8953	–4,356
Dy	$^6H_{15/2}$	$^4F_{9/2}$	4355	8388
Yb	$^2F_{7/2}$	$^2F_{5/2}$	17421	32,181

[a]ΔE_1 = [E(VB) – E(Ln^{3+})], [b]ΔE_2= [E(CB) – E(Ln^{3+}*)].

Using this model, one can rationalize the relative strengths of Ln sensitization in the NPs. Nd^{3+} with its $^4F_{3/2}$ level positioned at ΔE_2 = 24,196 cm^{-1} acts as a weak electron trap with a propensity for facile back electron transfer to the valence band of the photoexcited electron (from the electron-hole pair). This feature and the lowest ΔE_{phonon} value (5410 cm cm^{-1}) among the Ln^{3+} studied explains the extremely weak Nd^{3+} sensitization in $CsPbBr_3/NdCl_3$ and its absence in $CsPbCl_3/NdCl_3$ NPs. A similar mechanism operates for Sm^{3+} which explains the necessity to use time-gated photoluminescence spectroscopy to track the sensitized Sm^{3+} emission in $CsPbBr_3/SmCl_3$ and $CsPbCl_3/SmCl_3$ NPs (see Figures 5, 7). The placement of the $^6H_{15/2}$ level of the Dy^{3+} (ΔE_1 = 4355 cm^{-1}) makes it a weak hole trap that significantly limits the sensitization.

Eu^{3+} and Yb^{3+} act as moderate and strong electron traps respectively. Note the placement of Eu^{3+} and Yb^{3+} energy levels in the valence band continuum of the NP are not unusual. A similar positioning of the energy levels was used to rationalize the Eu^{3+} and Yb^{3+} sensitization in gallium nitride (GaN)[68] and ZnS hosts.[23, 41] The larger ΔE_1 value for Eu^{3+} (23,632 cm^{-1}), when compared to the Yb^{3+} (17421 cm^{-1}), signifies that the Eu^{3+} $^7F_0$ level is positioned deeper into the valence band continuum and thus should have a lower sensitization efficiency when compared to Yb^{3+}.

Scheme 1 Shows Different Fundamental Steps for an Eu^{3+} Sensitization Mechanism in $CsPbCl_3$ NPs

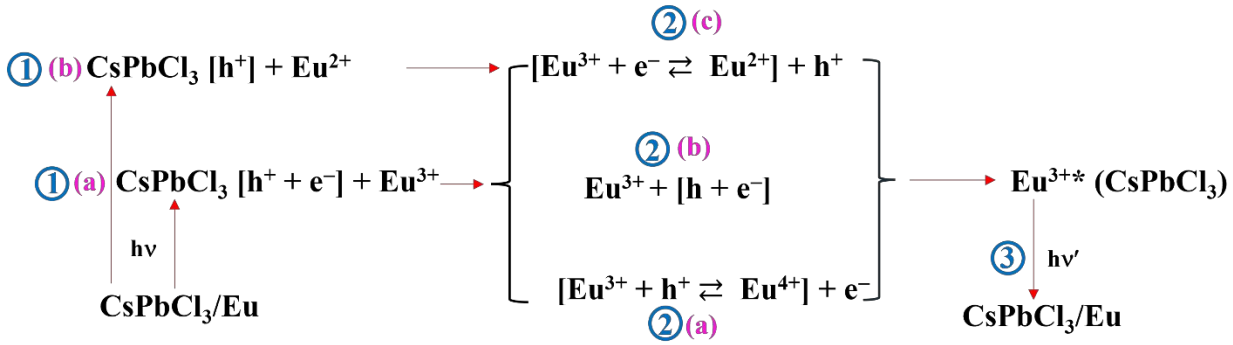

Scheme 1. The different fundamental steps leading to Eu^{3+} sensitization in $CsPbCl_3$ NPs is shown that include ① creation of excited state(s) in the NP, ② generation of Eu^{3+}* in NP, and ③ emission from Eu^{3+}*. It must be noted that charge trapping at the Eu^{3+} center [as shown in 2(a) and 2(c)] is not intended to represent a change in its redox state. The placement of e− (h+) outside square brackets indicates non-Ln centered charge carriers.

Optical excitation of the $CsPbCl_3$/Eu NPs generates excitons in the NP indicated by 1(a), as well as Eu^{2+} ground state indicated by 1(b). The direct excitation of Eu^{3+}*, although possible, is neglected and is believed to be minimal. Following optical excitation Eu^{3+}* in the NP is generated by electron-hole pair recombination or by conversion of the exciton via the 2(a), 2(b) and 2(c) processes. The rates for the trapping/detrapping processes in 2(a) and 2(c) as well as that for direct localization and conversion of the exciton are not known, however they generate the Eu^{3+}* excited level. Note that the Eu^{2+} state lies within the band gap of the $CsPbCl_3$. Figure 9 shows that the Eu^{3+} sites are embedded in the valence band so that the localized trap states in Scheme 1 (center)

are coupled with the quasi-continuum of valence band states which can autoionize and limit the efficiency of processes 2(a) – (c) and this facilitates luminescence sensitization following process (1b).

The Tb^{3+} presents an unusual case with its $^7F_6$ level positioned at $\Delta E_1 = -8953$ cm^{-1}, making it a strong hole trap. The $^5D_4$ level however lies above the conduction band, making autoionization a viable pathway to quench Tb^{3+} emission, which is not consistent with the efficient moderate Tb^{3+} emission observed in both $CsPbBr_3/TbCl_3$ and the moderate Tb^{3+} emission in $CsPbCl_3/TbCl_3$ NPs respectively. The time-gated excitation spectra, acquired by monitoring the Tb^{3+} emission at 545 nm (see Figures 5, 7), show a higher energy absorption band at 300-310 nm for the $CsPbBr_3/TbCl_3$ and $CsPbCl_3/TbCl_3$ NPs, in addition to the band at 397-400 nm which corresponds to the NP exciton absorption. This excitation band manifests in the NP absorption spectra also and likely correlates with a higher energy excited state of the perovskite NP (labeled as CB* in Figure 9). Note that the contribution of 4f-5d transition[12] in the generation of the higher energy transition cannot be entirely ignored and may well operate in concert with host sensitization. For this higher state the Tb^{3+} $^5D_4$ level would act as a moderate electron trap, thereby helping rationalize the observed Tb^{3+} emission sensitization. The origins of this anomaly and how it may be linked to the halide identity require further research.

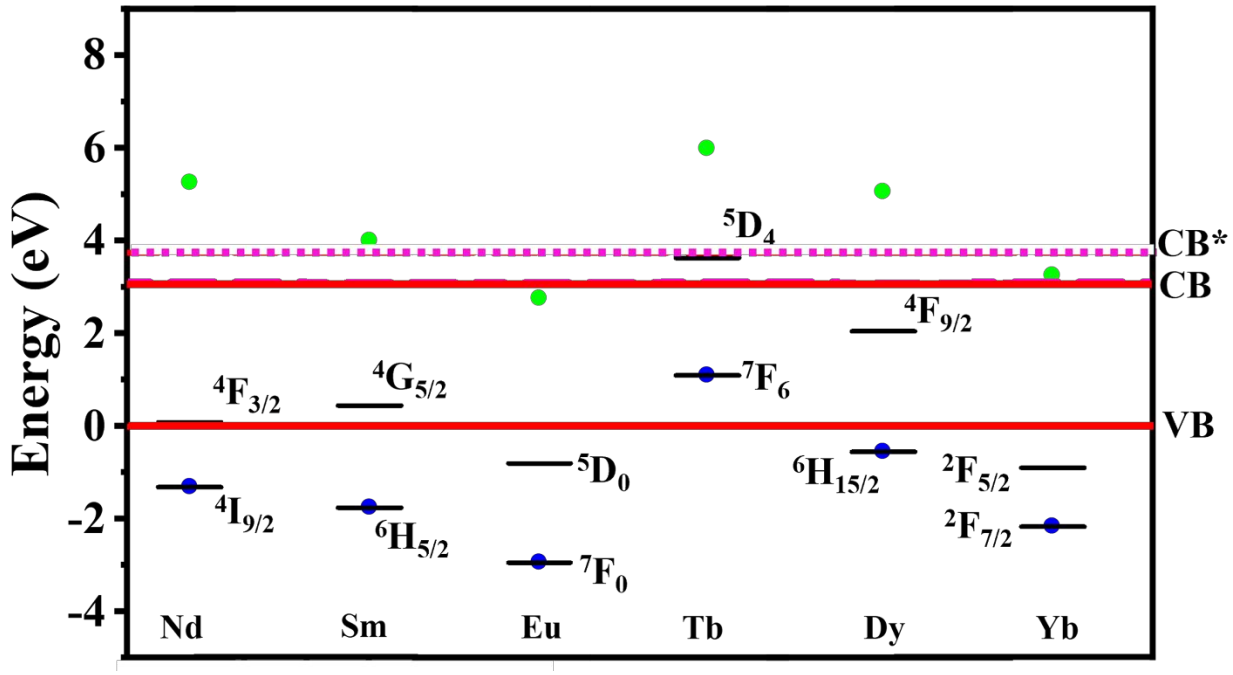

Figure 9. The relative energy levels of the Ln^{3+} [Ln = Nd, Sm, Eu, Tb, Dy, and Yb] ground and luminescent energy levels (black solid lines) with respect to the valence (VB) and conduction (CB) band (red solid lines respectively) of a $CsPbCl_3$ NP host is shown with a bandgap of 3.1 eV. The blue and green solid circles represent the Ln^{3+} and Ln^{2+} ground states respectively.

Other sensitization models, including Förster resonance energy transfer, were considered but do not account for the Ln^{3+} sensitization – largely because of the failure to correlate with spectral overlaps. This aspect is discussed in the SI and Figure S17.

Conclusion

This study presents a post-synthetic ion exchange strategy for room temperature doping of Ln^{3+} in $CsPbX_3$ NPs. Introduction of $LnCl_3$ [Ln = Nd, Sm, Eu, Tb, Dy, and Yb] salts to dispersions of $CsPbBr_3$ NPs initiates a halide exchange and the subsequent displacement of Pb^{2+} by Ln^{3+} leading to the formation of $CsPbBr_3/LnCl_3$ NPs. Electron microscopy experiments indicate the preservation of NP shape and dimension, however a crystal structure change occurs from the $CsPbBr_3$ to the $CsPbBr_3/LnCl_3$. X-ray photoelectron spectroscopy studies corroborate the electron microscopy results and indicate cation exchange with the Ln^{3+} successfully displacing Pb^{2+} via a

substitutional doping. Host sensitized Ln^{3+} emission in $CsPbBr_3/LnCl_3$ NPs was observed for all the Ln^{3+} investigated. The role of the halide exchange in dictating the Ln^{3+} sensitization was gauged by studying a similar post-synthetic doping strategy in $CsPbCl_3$ NPs. The Ln^{3+} sensitization was found to switch off for Nd^{3+} and Dy^{3+} doped $CsPbCl_3$ NPs, indicating that the post-synthetic modification of $CsPbBr_3$ by $LnCl_3$ is a better strategy to dope and observe sensitized Nd^{3+} and Dy^{3+} emission. A photophysical rationalization based on a combination of phonon emission and charge trapping is presented to rationalize the Ln^{3+} luminescence sensitization.

Experimental Details

Materials: Cesium carbonate (Cs_2CO_3, 99.9% trace metals basis), lead (II) bromide ($PbBr_2$, 99.999% trace metals basis), lead (II) chloride ($PbCl_2$, 99.999% trace metals basis), terbium (III) chloride ($TbCl_3$, anhydrous, 99.99% trace metals basis), europium (III) chloride ($EuCl_3$, anhydrous, 99.99% trace metals basis), samarium (III) chloride ($SmCl_3$, anhydrous, 99.9% trace rare earth metals basis), dysprosium (III) chloride ($DyCl_3$, anhydrous, 99.99% trace metals basis), neodymium (III) chloride ($NdCl_3$, anhydrous, ≥ 99.99% trace metals basis), ytterbium (III) chloride ($YbCl_3$, anhydrous, 99.9%), oleic acid (OA, technical grade, 90%), oleylamine (OAm, technical grade, 70%), octadecene (ODE, 90%), coumarin 153 (C153, 98%), IR-140, dimethyl sulfoxide (DMSO, ≥ 99.9%) and N, N-dimethylformamide (DMF, anhydrous, 98%) were purchased from Sigma Aldrich. Toluene, acetone, and methanol were purchased from Fisher. All chemicals were used without further purification.

Synthesis of $CsPbBr_3$ NPs: The synthesis of $CsPbBr_3$ NPs was adapted from the report of Kovalenko and coworkers.[2] Briefly, 0.2 g Cs_2CO_3, 0.70 ml OA and 10 ml ODE were loaded onto a 50 ml three neck round bottomed (RB) flask and flushed with argon for 1 hour at 120 ℃. The reaction was then sealed in an argon atmosphere and the temperature was raised to 150 ℃ for the

complete dissolution of Cs_2CO_3 to form Cs-oleate. The temperature of the reaction mixture was maintained at 150 ℃.

70 mg $PbBr_2$ and 5 ml ODE were loaded in a second three neck RB flask and flushed with argon at 120 ℃ for 1 hour and then sealed in the argon atmosphere. 0.5 ml OA and 0.5 ml OAm was then injected into the reaction mixture and the temperature was raised to 140 ℃. The reaction was allowed to continue until the complete dissolution of $PbBr_2$. 0.6 ml Cs-oleate was then rapidly injected and the reaction was quenched after 15 seconds by cooling the flask in an ice bath.

The crude reaction mixture was then centrifuged at 6500 rpm and 4 ℃ for 15 minutes. The supernatant was collected and a 1:1.5 volume/volume acetone was added and then further centrifuged at 10,000 rpm and 15 ℃ for 20 minutes to obtain the purified $CsPbBr_3$ NPs.

Synthesis of $CsPbCl_3$ NPs: The synthesis of $CsPbCl_3$ NPs was adapted from a report by Meijerink and coworkers.[71] Typically, 56 mg $PbCl_2$ and 5 ml ODE were loaded in a three neck RB and flushed with argon at 120 ℃ for 1 hour and then sealed in the argon atmosphere. 0.5 ml OA and 0.5 ml OAm was then injected into the reaction mixture and the temperature was raised to 190 ℃. When the temperature reached 190 ℃, 0.5 ml Cs-oleate was rapidly injected into the reaction mixture and cooled immediately in an ice bath to quench the reaction. The synthesized $CsPbCl_3$ NPs were purified by centrifuging the crude reaction mixture at 10,000 rpm and 15 ℃ for 20 minutes. The purified $CsPbCl_3$ NPs were dispersed in toluene.

Post-synthetic Modification and Ln^{3+} doping in Perovskite NPs: $CsPbBr_3$ NP dispersions in toluene (3.5 ml) were prepared with an optical density (O.D.) ≈ 0.8 at the first excitonic transition (485 – 490 nm). Next, a 45 mM $LnCl_3$ (Ln = Nd, Sm, Eu, Tb, Dy, and Yb) solution in anhydrous DMF was prepared. 0.25 ml of $LnCl_3$ solution was added to the 3.5 ml $CsPbBr_3$ NP dispersion and incubated overnight at room temperature. The final concentration of the Ln^{3+} in the NP

dispersion was 3.2 mM. The doped NPs can be purified by centrifuging at 8000 rpm for 20 minutes. A similar procedure was followed for doping Ln^{3+} in $CsPbCl_3$ NPs.

UV-Visible-NIR Absorption and Emission Spectroscopy: UV-Visible absorption spectra were collected on an Agilent 8453 spectrometer. UV-Visible, steady-state emission and excitation spectra were collected using a Horiba Jobin Yvon Fluoromax 3 fluorescence spectrometer with an integration time of 1 sec and a spectral resolution of 2 nm. The relative emission quantum yields (Φ_x) of the visible emitting samples were calculated with respect to coumarin 153 (C153) dissolved in methanol ($\Phi_r = 0.42$).[72] The NIR excitation and emission spectra were collected using a Horiba Nanolog fluorescence spectrometer with an integration time of 10 sec. For monitoring the Yb^{3+} excitation and emission profiles, a spectral resolution of 3 nm was used. An excitation and emission spectral resolution of 14.7 nm and 30 nm respectively, was used to monitor the Nd^{3+} luminescence. The relative emission quantum yields of the NIR emitting samples were calculated with respect to IR-140 in DMSO ($\Phi_r = 0.20$).[73] The emission quantum yields were calculated using equation 2:

$$\frac{\Phi_x}{\Phi_r} = \frac{A_r(\lambda_r)\, I_{ex}(\lambda_r)\, \eta_x^2 \int_0^\infty I_{em,x}(\bar{\upsilon})\, d\bar{\upsilon}}{A_x(\lambda_x)\, I_{ex}(\lambda_x)\, \eta_r^2 \int_0^\infty I_{em,r}(\bar{\upsilon})\, d\bar{\upsilon}} \quad (2)$$

where the subscripts x and r stand for sample and reference respectively, A is the absorbance at excitation wavelength (λ), I_{ex} is the intensity of the excitation light at the same wavelength, η is the refractive index (η = 1.496 for toluene, 1.327 for methanol and 1.479 for DMSO) and $I_{em}(\bar{\upsilon})$ is the emission intensity as a function of wavenumber ($\bar{\upsilon}$). The experiments were performed at room temperature.

Time-Gated Luminescence Spectroscopy: The time-gated excitation and emission spectra were collected on a Varian Cary Eclipse luminescence spectrometer. A 20 nm bandpass was used for

monitoring the excitation and emission spectra. The spectra were acquired using a delay time of 0.2 ms and a gate time of 5 ms. The delay time effectively removes the contribution from the nanosecond lived perovskite emission and the gate time helps monitoring only the long lived Ln^{3+} spectral features.

Time-resolved Luminescence Spectroscopy: The time-resolved emission decay profiles of the NPs were collected using the time-correlated single photon counting (TCSPC) method with a PicoHarp 300 TCSPC module (PicoQuant GmbH). The samples were excited using a picosecond diode laser at 378 nm (PiL037SM) with a repetition rate of 1MHz and the emission was collected at the magic angle. The full-width-at-half-maximum (FWHM) of the instrument response function (IRF) was ≤ 96 ps. The decays were fitted using an iterative reconvolution method with the fluorescence analysis software (FAST) from Edinburgh Instruments.

Transmission Electron Microscope (TEM) Imaging: The TEM images were acquired using a JEOL JEM-2100F operated at an acceleration potential of 200 kV. The samples were prepared by drop-casting a 10 µl NP dispersion in toluene onto a Cu TEM grid with ultra-thin carbon supporting film and dried in air.

X-ray Diffraction (XRD): Powder XRD patterns were collected from a Bruker D8 Discover XRD instrument equipped with a PSD (LYNXEYE) detector operated with an X-ray generator voltage and current of 40 kV and 40 mA respectively along with a Cu Kα source (λ = 1.54187 Å). Concentrated NP dispersions were drop-cast on a clean glass substrate and then dried before acquiring the spectra at room temperature. Data analysis was performed with the EVA XRD analysis software.

X-ray Photoelectron Spectroscopy (XPS): XPS spectra were collected using a Thermo Fisher Scientific ESCALAB 250 Xi. Samples were prepared by drop-casting a concentrated NP

dispersion in toluene on clean glass substrates and dried. Each spectrum was referenced to the peak energy position observed for adventitious carbon (C 1s 284.8 eV).

Associated Content

Supplementary Information

XPS spectra, absorption, photoluminescence spectra and maps, emission decays, XRD and Tables (PDF)

Conflict of Interest

The authors declare no competing financial interests.

Acknowledgements

The authors acknowledge U.S. Department of Energy (Grant no. ER46430) for supporting this work. We thank Prof. Alexander Star for allowing us to access the fluorometer in his lab and Dr. Xiaoyun He for her help in operating the instrument. We thank Prof. Jill E. Millstone for allowing us to use the time-gated photoluminescence spectrometer in her lab.

References

1. J. Shamsi, A. S. Urban, M. Imran, L. De Trizio and L. Manna, *Chem. Rev.*, 2019, **119**, 3296-3348.
2. L. Protesescu, S. Yakunin, M. I. Bodnarchuk, F. Krieg, R. Caputo, C. H. Hendon, R. X. Yang, A. Walsh and M. V. Kovalenko, *Nano Lett.*, 2015, **15**, 3692-3696.
3. Q. A. Akkerman, V. D'Innocenzo, S. Accornero, A. Scarpellini, A. Petrozza, M. Prato and L. Manna, *J. Am. Chem. Soc.*, 2015, **137**, 10276-10281.
4. F. Di Stasio, S. Christodoulou, N. Huo and G. Konstantatos, *Chem. Mater.*, 2017, **29**, 7663-7667.
5. H. Huang, M. I. Bodnarchuk, S. V. Kershaw, M. V. Kovalenko and A. L. Rogach, *ACS Energy Lett.*, 2017, **2**, 2071-2083.
6. L. M. Herz, *Annu. Phys. Rev. Chem*, 2016, **67**, 65-89.
7. W. Liu, Q. Lin, H. Li, K. Wu, I. Robel, J. M. Pietryga and V. I. Klimov, *J. Am. Chem. Soc.*, 2016, **138**, 14954-14961.
8. D. Parobek, B. J. Roman, Y. Dong, H. Jin, E. Lee, M. Sheldon and D. H. Son, *Nano Lett.*, 2016, **16**, 7376-7380.
9. H. Liu, Z. Wu, J. Shao, D. Yao, H. Gao, Y. Liu, W. Yu, H. Zhang and B. Yang, *ACS Nano*, 2017, **11**, 2239-2247.
10. M. N. An, S. Park, R. Brescia, M. Lutfullin, L. Sinatra, O. M. Bakr, L. De Trizio and L. Manna, *ACS Energy Lett.*, 2021, **6**, 900-907.
11. J.-C. G. Bünzli, *Chem. Rev.*, 2010, **110**, 2729-2755.
12. J.-C. G. Bünzli and C. Piguet, *Chem. Soc. Rev.*, 2005, **34**, 1048-1077.
13. A. A. Bol, R. v. Beek and A. Meijerink, *Chem. Mater.*, 2002, **14**, 1121-1126.

14. G. Pan, X. Bai, D. Yang, X. Chen, P. Jing, S. Qu, L. Zhang, D. Zhou, J. Zhu, W. Xu, B. Dong and H. Song, *Nano Lett.*, 2017, **17**, 8005-8011.
15. D. Zhou, D. Liu, G. Pan, X. Chen, D. Li, W. Xu, X. Bai and H. Song, *Adv. Mater.*, 2017, **29**, 1704149.
16. T. J. Milstein, D. M. Kroupa and D. R. Gamelin, *Nano Lett.*, 2018, **18**, 3792-3799.
17. D. M. Kroupa, J. Y. Roh, T. J. Milstein, S. E. Creutz and D. R. Gamelin, *ACS Energy Lett.*, 2018, **3**, 2390-2395.
18. Q. Li, Y. Liu, P. Chen, J. Hou, Y. Sun, G. Zhao, N. Zhang, J. Zou, J. Xu, Y. Fang and N. Dai, *J. Phys. Chem. C*, 2018, **122**, 29044-29050.
19. R. Sun, P. Lu, D. Zhou, W. Xu, N. Ding, H. Shao, Y. Zhang, D. Li, N. Wang, X. Zhuang, B. Dong, X. Bai and H. Song, *ACS Energy Lett.*, 2020, **5**, 2131-2139.
20. X. Zhang, Y. Zhang, X. Zhang, W. Yin, Y. Wang, H. Wang, M. Lu, Z. Li, Z. Gu and W. W. Yu, *J. Mater. Chem. C*, 2018, **6**, 10101-10105.
21. M. Zeng, F. Locardi, D. Mara, Z. Hens, R. Van Deun and F. Artizzu, *Nanoscale*, 2021, **13**, 8118-8125.
22. P. Mukherjee, R. F. Sloan, C. M. Shade, D. H. Waldeck and S. Petoud, *J. Phys. Chem. C*, 2013, **117**, 14451-14460.
23. G. H. Debnath, S. Rudra, A. Bhattacharyya, N. Guchhait and P. Mukherjee, *J. Colloid Interface Sci.*, 2019, **540**, 448-465.
24. G. H. Debnath, P. Mukherjee and D. H. Waldeck, *J. Phys. Chem. C*, 2020, **124**, 26495-26517.
25. S. Zhao, Y. Zhang and Z. Zang, *Chem. Commun.*, 2020, **56**, 5811-5814.
26. W. J. Mir, Y. Mahor, A. Lohar, M. Jagadeeswararao, S. Das, S. Mahamuni and A. Nag, *Chem. Mater.*, 2018, **30**, 8170-8178.
27. A. Kostopoulou, M. Sygletou, K. Brintakis, A. Lappas and E. Stratakis, *Nanoscale*, 2017, **9**, 18202-18207.
28. G. H. Debnath, Z. N. Georgieva, B. P. Bloom, S. Tan and D. H. Waldeck, *Nanoscale*, 2021, **13**, 15248-15256.
29. G. H. Ahmed, J. K. El-Demellawi, J. Yin, J. Pan, D. B. Velusamy, M. N. Hedhili, E. Alarousu, O. M. Bakr, H. N. Alshareef and O. F. Mohammed, *ACS Energy Lett.*, 2018, **3**, 2301-2307.
30. G. Almeida, L. Goldoni, Q. Akkerman, Z. Dang, A. H. Khan, S. Marras, I. Moreels and L. Manna, *ACS Nano*, 2018, **12**, 1704-1711.
31. C. C. Lin, K. Y. Xu, D. Wang and A. Meijerink, *Sci. Rep.*, 2017, **7**, 45906.
32. D. Briggs, *Practical surface analysis*, 1990, **1**, 595.
33. B. D. Padalia, W. C. Lang, P. R. Norris, L. M. Watson, D. J. Fabian and W. C. Price, *Proc. R. Soc. Lond. A.* , 1977, **354**, 269-290.
34. E. Talik, M. Kruczek, H. Sakowska, Z. Ujma, M. Gała and M. Neumann, *Journal of Alloys and Compounds*, 2004, **377**, 259-267.
35. C. Battistoni, G. Mattogno and E. Paparazzo, *Surf. Interface Anal.*, 1985, **7**, 117-121.
36. J. Huang, T. Lei, M. Siron, Y. Zhang, S. Yu, F. Seeler, A. Dehestani, L. N. Quan, K. Schierle-Arndt and P. Yang, *Nano Lett.*, 2020, **20**, 3734-3739.
37. Q. A. Akkerman, S. Park, E. Radicchi, F. Nunzi, E. Mosconi, F. De Angelis, R. Brescia, P. Rastogi, M. Prato and L. Manna, *Nano Lett.*, 2017, **17**, 1924-1930.
38. J. R. Dethlefsen, A. A. Mikhailovsky, P. T. Burks, A. Døssing and P. C. Ford, *J. Phys. Chem. C*, 2012, **116**, 23713-23720.

39. J.-C. G. Bünzli, *Interface Focus*, 2013, **3**, 20130032.
40. D. A. Chengelis, A. M. Yingling, P. D. Badger, C. M. Shade and S. Petoud, *J. Am. Chem. Soc.*, 2005, **127**, 16752-16753.
41. P. Mukherjee, C. M. Shade, A. M. Yingling, D. N. Lamont, D. H. Waldeck and S. Petoud, *J. Phys. Chem. A*, 2011, **115**, 4031-4041.
42. A. Chakraborty, G. H. Debnath, N. R. Saha, D. Chattopadhyay, D. H. Waldeck and P. Mukherjee, *J. Phys. Chem. C*, 2016, **120**, 23870-23882.
43. S. Petoud, G. Muller, E. G. Moore, J. Xu, J. Sokolnicki, J. P. Riehl, U. N. Le, S. M. Cohen and K. N. Raymond, *J. Am. Chem. Soc.*, 2007, **129**, 77-83.
44. G. H. Debnath, A. Chakraborty, A. Ghatak, M. Mandal and P. Mukherjee, *J. Phys. Chem. C*, 2015, **119**, 24132-24141.
45. P. Manna, A. Chakraborty, G. H. Debnath and P. Mukherjee, *J. Phys. Chem. Lett.*, 2017, **8**, 2794-2798.
46. P. Manna, G. H. Debnath, D. H. Waldeck and P. Mukherjee, *J. Phys. Chem. Lett.*, 2018, **9**, 6191-6197.
47. G. H. Ahmed, J. K. El-Demellawi, J. Yin, J. Pan, D. B. Velusamy, M. N. Hedhili, E. Alarousu, O. M. Bakr, H. N. Alshareef and O. F. Mohammed, *ACS Energy Lett.*, 2018, **3**, 2301-2307.
48. S. Paul, E. Bladt, A. F. Richter, M. Döblinger, Y. Tong, H. Huang, A. Dey, S. Bals, T. Debnath, L. Polavarapu and J. Feldmann, *Angew. Chem. Int. Ed.*, 2020, **59**, 6794-6799.
49. S. A. Egorov and J. L. Skinner, *J. Chem. Phys.*, 1995, **103**, 1533-1543.
50. S. A. Egorov and J. L. Skinner, *J. Chem. Phys.*, 1996, **105**, 10153-10155.
51. A. Beeby, I. M. Clarkson, R. S. Dickins, S. Faulkner, D. Parker, L. Royle, A. S. deSousa, J. A. G. Williams and M. Woods, *J. Chem. Soc., Perkin Trans. 2*, 1999, 493-503.
52. V. L. Ermolaev and E. B. Sveshnikova, *Chem. Phys. Lett.*, 1973, **23**, 349-354.
53. K. K. Pukhov, F. Pelle and J. Heber, *Molecular Physics*, 2003, **101**, 1001-1006.
54. W. T. Carnall, P. R. Fields and K. Rajnak, *J. Chem. Phys.*, 1968, **49**, 4412-4423.
55. W. T. Carnall, P. R. Fields and K. Rajnak, *J. Chem. Phys.*, 1968, **49**, 4424-4442.
56. W. T. Carnall, P. R. Fields and K. Rajnak, *J. Chem. Phys.*, 1968, **49**, 4443-4446.
57. W. T. Carnall, P. R. Fields and K. Rajnak, *J. Chem. Phys.*, 1968, **49**, 4447-4449.
58. W. T. Carnall, P. R. Fields and K. Rajnak, *J. Chem. Phys.*, 1968, **49**, 4450-4455.
59. S. Rudra, M. Bhar and P. Mukherjee, *J. Phys. Chem. C*, 2019, **123**, 29445-29460.
60. W. W. Anderson, *Phys. Rev.*, 1964, **136**, A556-A560.
61. N. Jing-hua, H. Rui-nian, L. Wen-lian, L. Ming-tao and Y. Tian-zhi, *J. Phys. D: Appl. Phys.*, 2006, **39**, 2357-2360.
62. T. Gregorkiewicz, D. T. X. Thao, J. M. Langer, H. H. P. T. Bekman, M. S. Bresler, J. Michel and L. C. Kimerling, *Phys. Rev. B*, 2000, **61**, 5369-5375.
63. I. Tsimperidis, T. Gregorkiewicz, H. H. P. T. Bekman and C. J. G. M. Langerak, *Phys. Rev. Lett.*, 1998, **81**, 4748-4751.
64. K. Thonke, K. Pressel, G. Bohnert, A. Stapor, J. Weber, M. Moser, A. Molassioti, A. Hangleiter and F. Scholz, *Semicond. Sci. Technol.*, 1990, **5**, 1124-1131.
65. M. A. J. Klik, T. Gregorkiewicz, I. V. Bradley and J.-P. R. Wells, *Phys. Rev. Lett.*, 2002, **89**, 227401-227401-227401-227404.
66. W. J. Chang, S. Irgen-Gioro, S. Padgaonkar, R. López-Arteaga and E. A. Weiss, *J. Phys. Chem. C*, 2021, **125**, 25634-25642.
67. P. Dorenbos, *J. Alloys Compd.*, 2009, **488**, 568-573.

68. P. Dorenbos and E. van der Kolk, *Appl. Phys. Lett.*, 2006, **89**, 061122-061121-061122-061123.
69. C. K. Jørgensen, *Modern Aspects of Ligand Field Theory*, North-Holland, Amsterdam, 1971.
70. M. V. Kovalenko, L. Protesescu and M. I. Bodnarchuk, *Science*, 2017, **358**, 745-750.
71. K. Xu, J. F. Vliem and A. Meijerink, *J. Phys. Chem. C*, 2019, **123**, 979-984.
72. J. E. Lewis and M. Maroncelli, *Chem. Phys. Lett.*, 1998, **282**, 197-203.
73. S. Hatami, C. Würth, M. Kaiser, S. Leubner, S. Gabriel, L. Bahrig, V. Lesnyak, J. Pauli, N. Gaponik, A. Eychmüller and U. Resch-Genger, *Nanoscale*, 2015, **7**, 133-143.